Journal of Visualization, Vol. 4, No. 1 (2001) 61-72

Use of the Wake of a Small Cylinder to Control Unsteady Loads on a Circular Cylinder

Bouak, F.* and Lemay, J.*

* Laboratoire de Mécanique des Fluides, Département de génie mécanique, Université Laval, Ste-Foy (Québec) G1K 7P4, Canada.

Received 13 October 2000.
Revised 10 January 2001

***Abstract*:** Simultaneous measurements of lift and drag forces have been performed in order to study passive control of unsteady loads induced on a circular cylinder. For this purpose, an aerodynamic balance has been developed. The balance, developed for a cylinder of 25.4 mm in diameter, was designed to operate in the subcritical regime (Re = 32000). This instrument is characterized by its sensitive element that forms a small central part of the cylinder. The static and dynamic calibrations of the balance show the appropriateness of the present design. Moreover, qualification experiments carried out with a single cylinder gave results (mean and rms values of the lift and drag coefficients) that are in good agreement with those found in the literature. The purpose of this paper is to present a passive control experiment performed by means of the wake of a smaller cylinder interacting with a larger one. Firstly, a parametric study was performed by varying the following: i) the diameter d_s of the small cylinder for one large cylinder diameter d (7 values in the range $0.047 \le d_s/d \le 0.125$); ii) the center-to-center spacing S/d (11 values in the range $1.375 \le S/d \le 2.5$); and iii) the stagger angle a ($0^\circ \le a \le 90^\circ$ with a fine angular step Da for $a \le 15^\circ$). A maximum mean drag reduction of about 48% is achieved. At $a = 4^\circ$ to 8°, one can observe a peak of mean lift coefficient. Then unsteady fluid forces, vortex shedding frequency and flow pattern were systematically investigated for the small cylinder having a diameter d_s = 2.4 mm (0.094 d). Reductions of 78% and 56% of the rms lift and drag fluctuations respectively were obtained with the small cylinder placed at a slight stagger angle in the range $6^\circ < a < 9^\circ$. This leads to an instantaneous force vector that exhibits more steadiness both in angle and amplitude. Moreover, at these stagger angles, the energy of the lift fluctuations at the shedding frequency is significantly reduced compared to the single cylinder case.

***Keywords*:** cylinder, drag, flow control, balance.

1. Introduction

Flow around circular cylinders has been to extensively researched in a wide range of engineering disciplines (see Zdravkovich, 1997 and Niemann and Hölscher, 1990). The different studies show that this flow configuration has many engineering applications and still presents one of the challenges in fluid mechanics. Indeed, the aerodynamic parameters such as the unsteady drag and lift forces, instantaneous pressure field, vortex shedding phenomena, mechanisms governing the wake formation and its downstream evolution, and 3D effects (spanwise variations) are interrelated and influenced by a large number of factors, including Reynolds number, surface roughness, external flow conditions (turbulence level, mean shear, etc.) and geometry (proximity of a flat wall or another surface, interaction between several cylinders, length to diameter ratio, etc.). To control one of the aforementioned unsteady phenomena, one must carefully measure the fluctuating physical quantities of interest.

The aim of the present study is to investigate the problem of controlling or manipulating the unsteady loads

induced on a circular cylinder of diameter d. The passive flow control is performed by means of the wake of a small cylinder d_s interacting with the larger one. The objective was to alter the separation process with the shear layers coming from the upstream small cylinder. Igarashi (1994, 1997 and 2000) and Tsutsui and Igarashi (2000) studied heat transfer enhancement and drag reduction of a square prism and drag reduction of a circular cylinder controlled by a small rod set upstream. Lesage and Gartshore (1987) investigated the effect of placing a small cylinder in the stagnation line upstream of a bluff body (a flat plate, a square and a circular cylinder). They obtained a significant mean drag reduction for all bluff body shapes. The fluctuating lift force on the circular cylinder was reduced by the small cylinder at high Reynolds number ($\geq$ 80000). In the case of S/d = 2.55 and d_s = 3.2 mm (d_s/d = 0.125), Bouak and Lemay (1998) show that lift and drag coefficients and shedding intensity differ significantly from the single cylinder case. For example, a mean drag reduction of 32%, a peak of mean lift coefficient, a decrease in the rms lift fluctuations and Strouhal number modification have been observed at certain locations of the small cylinder. For the purpose of these experiments, an aerodynamic balance was used, allowing the simultaneous measurement of both the mean and fluctuating lift and drag forces.

2. Experimental Setup

Figure 1 shows a schematic diagram of the cylinders configurations and the different parameters under investigation. Seven small cylinders of diameters varying from 1.19 mm to 3.2 mm, corresponding to $3d/64$ to $d/8$ respectively, were used. Each small cylinder covers a range of center-to-center spacing S/d from 1.375 to 2.5. A turntable, flush with the floor of the tunnel and supporting both cylinders, allowed the stagger angle α to be adjusted from 0° to 90° relative to the freestream velocity vector. By varying this angle and the spacing S/d, a wide range of staggered configurations were possible. The effect of spacing and small cylinder diameter on the flow characteristics were investigated.

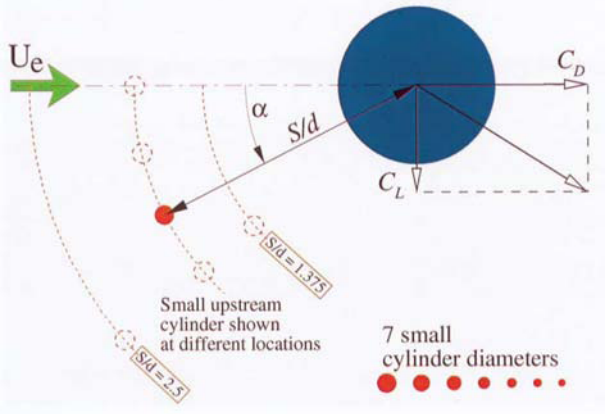

Fig. 1. Schematic of the two-cylinder experimental setup; $0.047 \leq d_s/d \leq 0.125$; $1.375 \leq S/d \leq 2.5$.

The experiments were carried out in a closed-loop wind tunnel characterized by a freestream turbulence level of 0.2%. This facility has a 1.5 m long test section, with a 0.90 m high by 0.92 m wide quasi-octagonal cross-section. The freestream velocity of the wind tunnel was constant and adjusted to 20 m/s, yielding a Reynolds number based on the larger cylinder diameter of about 32000. Moveable circular end plates of $9d$ in diameter allowed an aspect ratio of 17 to be fixed. As pointed out by several authors (cf. Moeller, 1982 and West and Apelt, 1993), an aspect ratio that is larger than 10 is found to give "long" cylinder results at its mid-span section. This conclusion has also been confirmed by our measurements. For the purpose of these experiments, an aerodynamic balance was used, allowing the simultaneous measurements of the fluctuating lift and drag forces (see Bouak and Lemay, 1998 and Bouak, 1999 for more details). The signals coming from the balance were simultaneously sampled with a 16 channel 2570 signal analyzer from BAKKER Electronics. For this experiment, 64 samples of 4096 data per channel were used for the computation of the statistical quantities of interest. The sampling frequency was set at 5 ksample/second and the anti-aliazing filters set to a cut-off frequency of 2 kHz. This resulted in a precision of around 12% on the autospectral density estimates that were computed over 64 contiguous segments of 4096 data points. These spectra are thus characterized by a cut-off frequency of 2.5 kHz and Df = 1.22 Hz. A smoke-wire visualization technique was also used in order to study the flow behavior around the cylinders.

For this purpose, the flow velocity was adjusted to 3 m/s. Four synchronized flash lamps (0.2 J each lamp during 2.5 μs) were used with Tmax-400 Kodak film.

3. The Aerodynamic Balance

Figure 2 shows a schematic of the aerodynamic balance developed to provide the simultaneous measurement of both the mean and fluctuating lift and drag forces. It uses internal strain gauges fixed on a cantilever beam, which consists of two sections perpendicular to one another. A sensitive element (25.4 mm in diameter by 25.4 mm long), forming a small central part of the cylinder, is attached to the beam. When exposed to the flow field, this element allows the beam to bend in both orthogonal directions under the action of the aerodynamic load. The cantilever beam then provides two orthogonal forces that can be combined together to compute the mean and fluctuating lift and drag forces. A complete strain gauge bridge is mounted on each section of the beam, providing temperature compensation and optimum sensitivity.

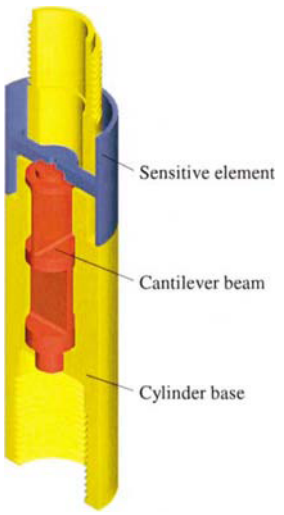

Fig. 2. Schematic of the aerodynamic balance allowing the simultaneous measurement of mean and fluctuating lift and drag forces.

The design calculations indicate a sensitivity of 4 mV/gram-force (assuming a gain of 1000 and a gauge factor of 2.3) and natural frequencies of approximately 300 and 350 Hz for the upper and lower sections of the beam respectively. The design procedure is described in more detail in Bouak and Lemay (1998) and Bouak (1999).

3.1 Calibration Procedure

Static calibration: The sensitivity obtained for the balance used is 5.6 mV/gram-force for the upper section of the beam and 4.5 mV/gram-force for the lower section. Moreover, the linearity of the instrument is excellent, with a regression coefficient of 0.9999. The calibration results confirm the design estimate.

Dynamic Calibration - Frequency Response: The goal of the dynamic calibration is to determine the gain factor of the frequency response of the balance. The dynamic calibration is performed using an electrodynamic shaker, which vibrates a short cylinder equipped with a balance. The input (acceleration a) is recorded with an accelerometer and the output is the bridge voltage of one section of the beam (representing the relative displacement z). The electrodynamic shaker is excited with a sinusoidal signal of frequency f. The gain factor at this frequency is given by the ratio: $|H(f)| = z_{\text{rms}}/a_{\text{rms}}$.

The rms values are measured with a Philips PM-2535 system multimeter (6 1/2 digit). The frequency response function (gain factor) is obtained by varying the frequency over the range of interest $0 \leq f \leq 500$ Hz. Each section must be calibrated independently.

As shown in Fig. 3, the results are found to be in excellent agreement with the theoretical model. The undamped natural frequencies and the damping ratios are found to be: $f_n = 265$ Hz and $\chi = 0.0035$ for the upper section of the beam, and $f_n = 261$ Hz and $\chi = 0.0042$ for the lower section. These values must be determined for each individual balance because f_n and χ are dependent on the actual beam geometry. For the different balances

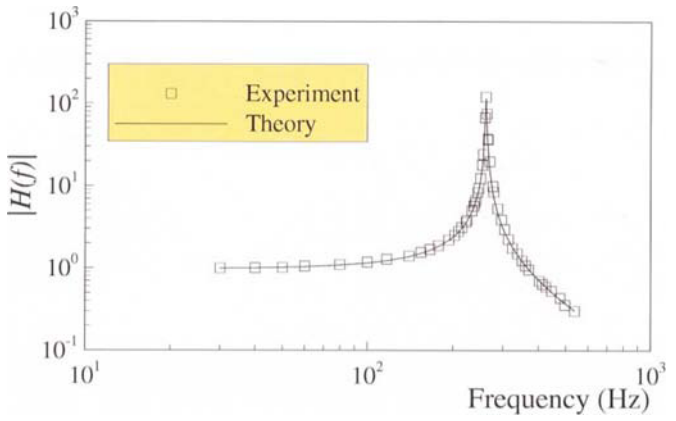

Fig. 3. Gain factor obtained from the dynamic calibration of the lower section of the beam.

tested, the measured natural frequencies ranged from 250 to 280 Hz.

Dynamic Calibration - Compensation Procedure: The numerical compensation procedure is based on the inverse of the frequency response combined with a 10th order Butterworth filter (Fig. 4). Such a procedure extends the dynamic capabilities of the balance. Moreover, since the instrument is an under-damped second order system, the signals are numerically damped at the natural frequency.

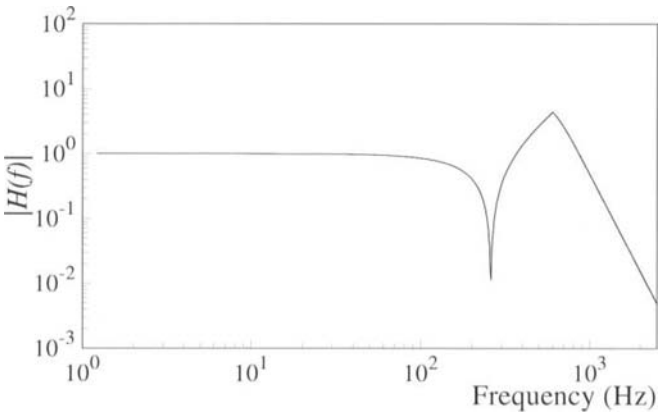

Fig. 4. Compensation-filter function.

3.2 Validation of the Balance Response

Before analyzing the performance of the balance, we first of all subjected the balance to a series of preliminary tests (verify that the flow was not perturbed by the small amplitude displacement of the sensitive element, the influence of the junction between this element and the fixed part, etc.). These tests are described in more detail in Bouak and Lemay (1998) and Bouak (1999).

In order to illustrate the application of the balance, a few measurements are presented using a single cylinder in the range $16000 \leq Re \leq 38000$. All the results were filtered using the compensation-filter function (Fig. 4) corresponding to each section of the beam. Figure 5 shows an example of the unsteady lift and drag coefficients measured simultaneously. These data were obtained with the balance orientated at $q = 0°$, a position corresponding to the case where the upper and lower sections of the beam measured respectively the lift and drag forces.

A decomposition of the two signals from the upper and lower sections of the beam allows one to determine the lift and drag forces for any angle q. The forces computed from the combination of both signals must be independent of the orientation q. This point is very important if one aims for example to use several balances in multiple cylinder configurations. Averaging the results for $Re = 32000$ over all the values of q, the following values were obtained: $C_L = 0$, $C_D = 1.2$, $C_l' = 0.47$, $C_d' = 0.12$ and St = 0.2. These results are in good agreement with those reported in the literature, generally using different measurement techniques (e.g. pressure measurements instead of simultaneous lift and drag measurements). This conclusion could be generalized to the various quantities computed

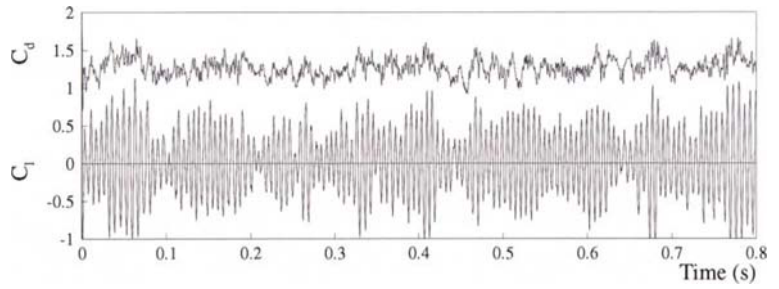

Fig. 5. Unsteady lift and drag coefficients for a single cylinder; Re = 32000.

from the unsteady lift and drag forces (autospectral density functions, etc.), which confirms the appropriateness of the aerodynamic balance.

4. Passive Control: Results and Discussion

4.1 Parametric Study Results

The lift and drag coefficients of the downstream cylinder (the larger one) at Re = 32000 are shown in Fig. 6 for seven different diameters of the upstream small cylinder and a center-center spacing S/d = 1.5 and 2.5. The results indicate that C_L and C_D are strongly affected over specific ranges of center-center spacing, small cylinder diameter and stagger angle.

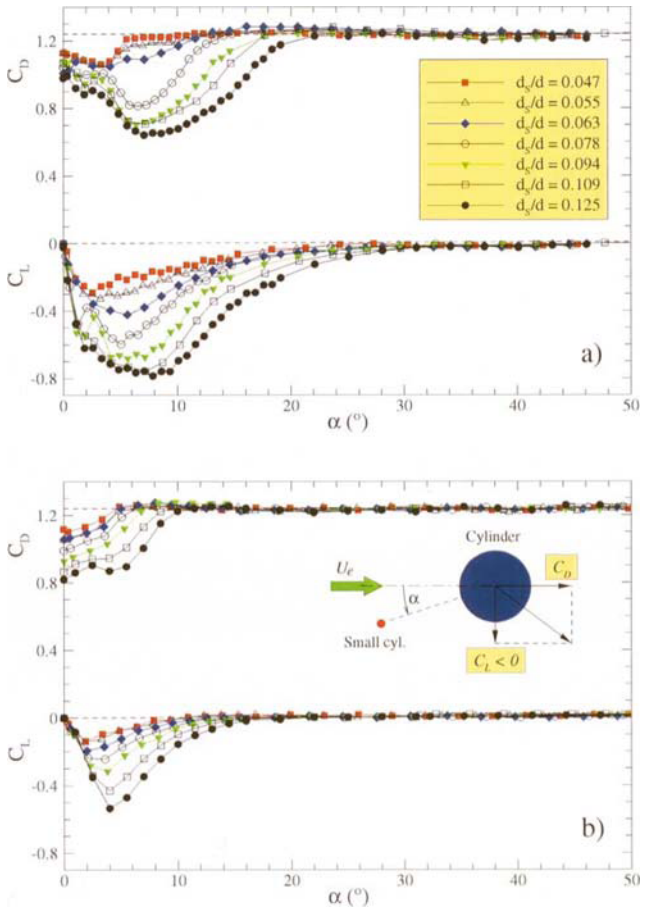

Fig. 6. Mean lift and drag coefficients as a function of the stagger angle; $0.047 \leq d_s/d \leq 0.125$; dashed lines: single cylinder case; a) S/d = 1.5; b) S/d = 2.5.

First of all, it is obvious to notice that, for each value of spacing, the mean drag coefficient, C_D, decreases with the increase of the small cylinder diameter, d_S. In addition, in the lowest range of S/d and a values (Fig. 6a), C_D is a minimum not at tandem arrangement as would be expected but at $a = 2^\circ$ to 8° depending on the diameter of small cylinder. Moreover, a_{min} decreases and tends to 0 as d_S reduces. On the other hand, for $S/d = 2.5$ (Fig. 6b), the minimum value of C_D always occurs at tandem arrangement ($a = 0^\circ$) for all values of d_S. For $d_S/d = 0.125$, the maximum drag reduction values, $(C_{D0} - C_D)/C_{D0}$, reaches 48%, C_{D0} being the mean drag coefficient of a single cylinder. For equivalent drag coefficients, the drag force induced on the small cylinder will be 12.5% of the large

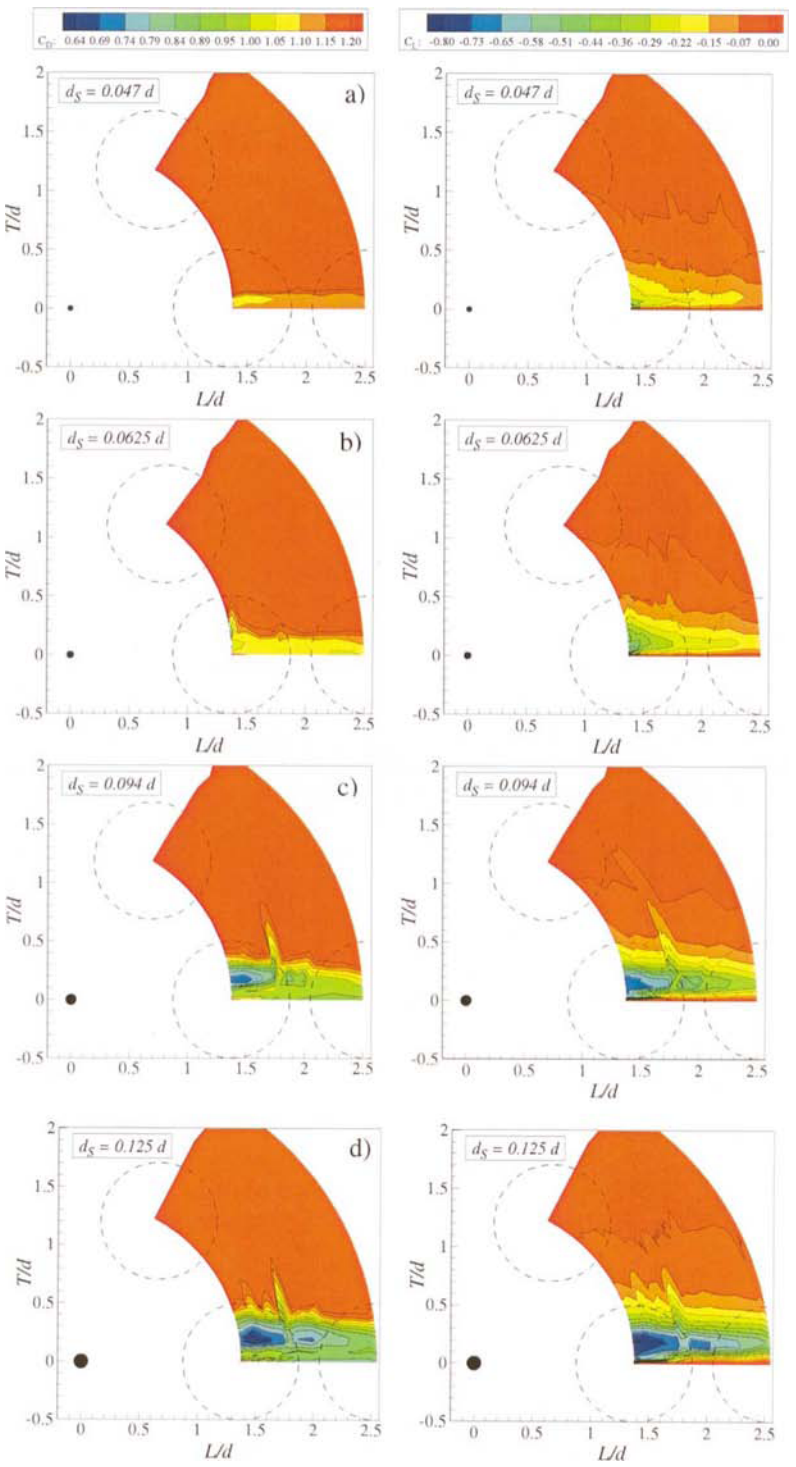

Fig. 7. Contour plots of mean drag (left) and lift (right) coefficients; $1.375 \le S/d \le 2.5$; a) $d_S/d = 0.047$; b) $d_S/d = 0.0625$; c) $d_S/d = 0.094$; d) $d_S/d = 0.125$.

cylinder drag (0.125 being d_s/d the ratio of the two diameters). Thus, the overall balance yields a 35.5% maximum mean drag reduction. Previously, with the same small cylinder but S/d = 2.55, Bouak and Lemay (1998) have reduced the total mean drag of a cylinder to approximately 19.5%.

Another important feature is the negative peak observed on the distribution of the mean lift coefficient, C_L, in the lowest range of α ($2^\circ \leq \alpha \leq 8^\circ$). For certain values of spacing and small cylinder diameter, this peak can reach a value of –0.8. And finally, the third noticeable feature is the coincidence of the C_L peak with the minimum drag coefficient at small value of spacing. For example, with S/d = 1.375 (the smallest spacing) and d_s/d = 0.125 (the larger small cylinder), the corresponding C_L peak and minimum drag lead to a large resultant force coefficient (= 1.1, which means as high as 89% of the value of the single cylinder), oriented at an angle of 50° and directed downwards.

A better insight into the variations of the force coefficients for various diameters and arrangements can be obtained by representing curves of constant coefficients. These curves were obtained by interpolation between the measured values of drag and lift coefficients and are shown in Fig. 7.

The experimental results for the Reynolds number 32000 are presented in a $L/d - T/d$ (Longitudinal and Transverse spacing) coordinate systems. The location and dimension of the small cylinder are shown on the lower left corner of each plot (at scale); the dashed circles represent the boundary locations covered by the larger cylinder.

One can easily note from Fig. 7 that the small cylinder always has the effect to reduce the drag force and to induce a lift force for all values of the center-center spacing considered in the present study. Moreover, it is interesting to notice that the contour plots of mean lift coefficient show a small positive repulsive force ($C_L > 0$) for all stagger angles higher than a specific value which is a function of d_s and S. All other staggered arrangements have a negative lift directed toward the axis of the upstream small cylinder wake. On the other hand, the corresponding contour plots of mean drag coefficient are less wide in the transverse direction which means that C_D reaches the value of the single cylinder case at a smaller stagger angle value than for the lift. The most important feature is that, for $d_s/d \geq 0.078$ (the four larger diameters), there are two separate maximum lift coefficients. The first one occurs at a small stagger angle (α = 1° to 2°), and the other at α = 4° to 7.4°. One must also note that both peaks are observed, as shown in Fig. 7 (see also Fig. 6a) in the range $1.375 \leq S/d \leq 1.625$ (the three smaller spacings), indicating that they have two different physical origins. The contour plots of mean drag coefficient are similar to that of the mean lift coefficient. It shows also two regions of minimum drag, occurring at the same ranges of d_s/d and S/d as the maximum lift coefficient.

4.2 Unsteady Results of the Case: d_s/d = 0.094 and S/d = 1.5

4.2.1 rms lift and drag coefficients

For this case, Figure 6 shows that the negative mean lift coefficient occurs at $4.2^\circ < \alpha < 6.5^\circ$ (corresponding to a transverse spacing T/d between 0.11 and 0.17). In this range of stagger angle, the maximum C_L (in absolute value)

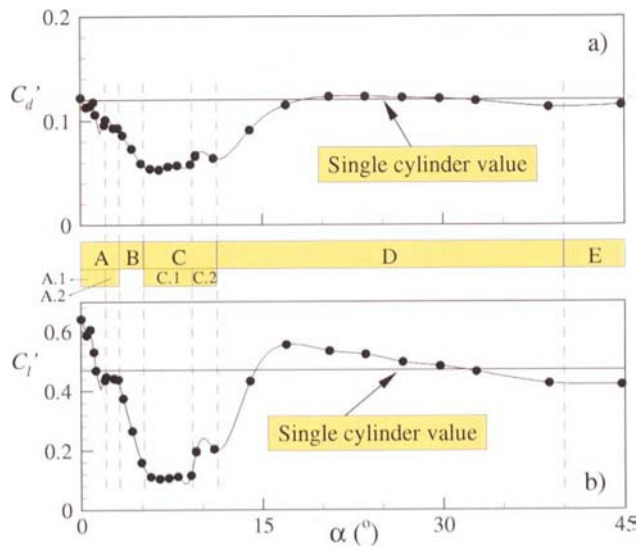

Fig. 8. rms lift and drag coefficients as a function of the stagger angle.

coincides with a minimum value of C_d' and C_l' respectively, the rms drag and lift coefficients (Fig. 8). The decreases of C_l' and C_d' at $a = 6.5^\circ$ correspond to reductions of about 78% and 56% respectively when compared with the single cylinder case. Moreover, the rms values are lower than those corresponding to a single cylinder at the same Reynolds number, in the range $a < 20^\circ$ for C_d' and in a large range of a for C_l' (except in the range $0^\circ < a < 1.2^\circ$ and $15^\circ < a < 32^\circ$ where C_l' is greater). Indeed, at tandem arrangement ($a = 0^\circ$), C_l' reaches 0.64 which is 36% greater than the value of a single cylinder. Another important feature of mean and rms drag and lift coefficients curves (Fig. 6 and Fig. 8) is the presence, at $a = 2^\circ$, of a discontinuity (kink) yielding a second maximum value of C_L and another minimum value of C_D and C_l'. According to these observations, flow regimes A to E have been identified as shown in Fig. 8, depending on the value of C_D, C_L and C_l'. These flow regimes will be defined in the next sections and flow visualization analysis will help in understanding these points.

4.2.2 Power spectrum of lift coefficient and total force vector

Figure 9 shows the autospectral density function of the lift force fluctuations for the case of the single cylinder as well as for the two-cylinder arrangements (cases $a = 0^\circ$, 2.7° and 17°). The peak observed on each curve is the one that is used to determine the Strouhal number corresponding to the vortex shedding frequency, f_s. This peak, which is sharp and easy to identify, contains the most significant part of the energy content of the signal. Indeed, Figure 9 must be analyzed keeping in mind the distribution of the rms lift coefficient (cf. Fig. 8b), as the integral of these

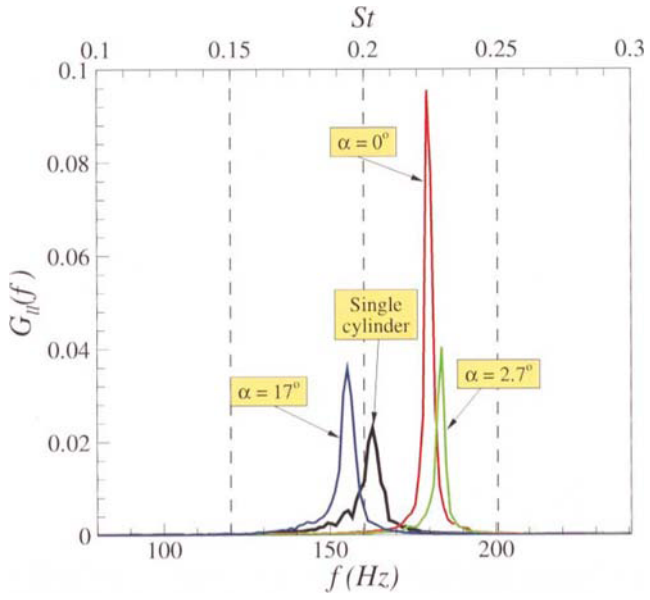

Fig. 9. Autospectral density functions for of C_l' different configurations. For $a = 6.5^\circ$, $G_{ll}(f) \approx 0$ and for $a = 45^\circ$ $G_{ll}(f) \approx$ single cylinder case.

curves must be equal to the variance of the signal, by Parseval's theorem.

We first observe that, for $a = 0^\circ$ (tandem arrangement), the Strouhal number St is larger than the value corresponding to the single cylinder case. One can also surmise that this Strouhal number increase could be attributed to the decrease in the velocity of the local flow approaching the downstream cylinder. Moreover, the spectral peak for this configuration is larger by 316% and is narrower than the single cylinder case, indicating that the shedding phenomena is more centered on f_s and more intense. When integrated, this larger peak results in an increase of the rms value, as previously pointed out from the analysis of Fig. 8. The periodic regularity of the total force vector is well illustrated in Fig. 10a.

It is important to note that the case $a = 6.5^\circ$ (corresponding to $C_{L\max}$ and $C_{l'\min}$) is not presented in Fig. 9 because $G_{ll}(f) \approx 0$. Therefore, there exists no distinct frequency component. This indicates that the instantaneous lift force is much more steady for this cylinder arrangement. This can be clearly seen in Fig. 10c), which shows a typical time sequence of the total force vector. The downstream cylinder is subjected to almost steady loading. This particular aspect is very important because it illustrates the fact that the instantaneous force vector exhibits more steadiness both in angle and amplitude. This behavior is also interesting from the flow control viewpoint.

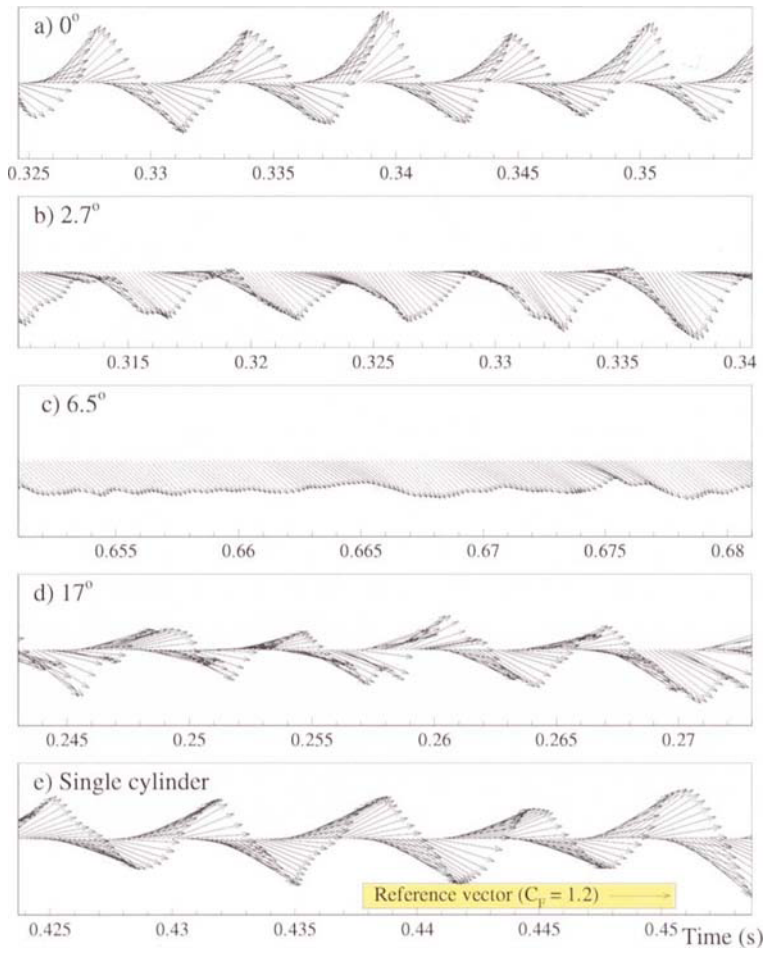

Fig. 10. Resultant force vector as a function of time; a) $a = 0^\circ$; b) $a = 2.7^\circ$; c) $a = 6.5^\circ$; d) $a = 17^\circ$; e) single cylinder.

4.2.3 Flow visualization and classification of controlled flow patterns

Flow visualizations were used to provide more insight into the analysis achieved in previous paragraphs. Flow patterns corresponding to $a = 0^\circ$, 4.5°, 7.5° and 10.5° are shown in Fig. 11 to Fig. 14 respectively.

For $a = 0^\circ$, Figure 11 clearly indicates the reattachment of the small cylinder shear layers to the front surface of the downstream cylinder. The two cylinders work just as a single body connected by the stagnant region in the gap. Therefore, it results, if compared to the single cylinder case (no control case), in a decrease of C_D, and an increase of both C_l' (cf. Fig. 8) and St (cf. Fig. 9). The stagnant region acts such that it reduces the stagnation

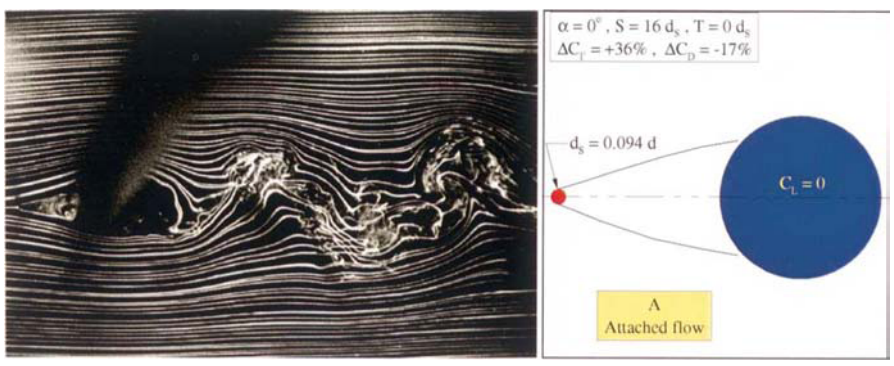

Fig. 11. Smoke-wire flow visualization and schematic of the flow pattern A (attached flow regime); configuration $S/d = 1.5$, $a = 0^\circ$.

pressure on the downstream cylinder. For $a = 2.5^\circ$, the wake deviates upwards, indicating downward lift, which is in accordance with Figs. 6 and 7. It can also be clearly still noticed that the two shear layers of the small cylinder, as in the previous arrangement, are attached to the front surface of the downstream cylinder. According to these observations, Pattern A is defined as the flow in the range from $a = 0^\circ$ to the stagger angle at which shear layers of the small cylinder are no longer attached on the downstream cylinder. Before the Karman vortex shedding begins to be clearly noticeable (i.e., in the transition region between Pattern A and the following one), the flow is bi-stable (region A. 2 in Fig. 8), which results in a discontinuity in lift and drag coefficients curves.

For $a = 4.5^\circ$ (Fig. 12), the upward deviation of the wake is more obvious. We also clearly notice the formation of Karman vortex streets behind both cylinders and the splitting of the small cylinder wake. Hence, Pattern B is generated from the range of a at which the small cylinder begins to shed to the end of the small wake splitting.

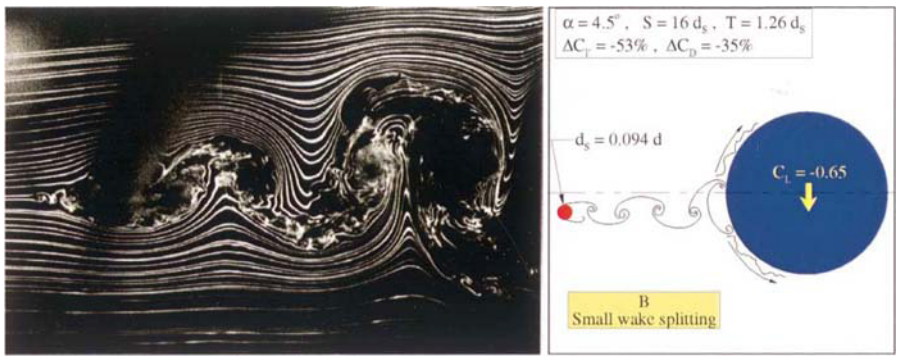

Fig. 12. Smoke-wire flow visualization and schematic of the flow pattern B (small-wake splitting flow regime); configuration $S/d = 1.5$, $a = 4.5^\circ$.

For $a = 7.5^\circ$ (Fig. 13), the upwards deviation is more pronounced, indicating a large downward lift, which is in accordance with Fig. 6. We also clearly notice that for this angle and the following ones, the two shear layers issuing from the small cylinder completely bypass the upward side of the large cylinder. This behavior results in an asymmetrical flow around the downstream cylinder and a strong boundary layer interaction from its stagnation point. The asymmetrical boundary layers are apparently more stable as regards to the separation point, as indicated by the large decrease of the rms lift coefficient (Fig. 8b) and the steadiness of the total force vector observed in Fig.10 (note that for $a = 6.5^\circ$ the flow pattern is the same as for $a = 7.5^\circ$). Pattern C. 1 is defined as the flow regime in which small wake merging occurs inducing a strong perturbation of boundary layer from the stagnation point.

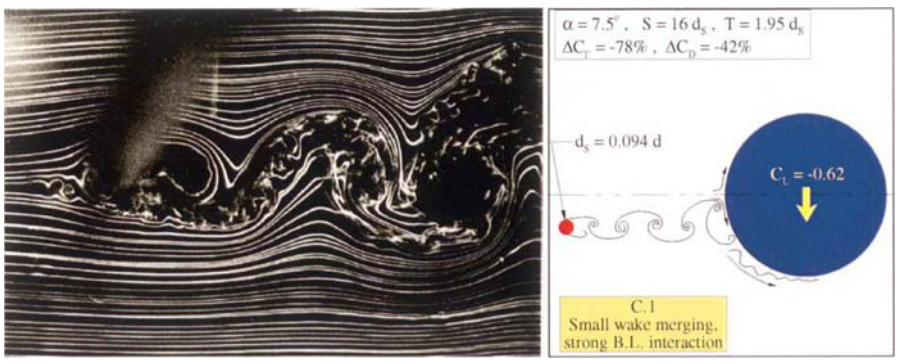

Fig. 13. Smoke-wire flow visualization and schematic of the flow pattern C.1 (small wake merging flow regime with strong boundary layer interaction from the stagnation point); configuration $S/d = 1.5$, $a = 7.5^\circ$.

One must notice that the variation of lift and drag coefficients (mean and rms) as a function of the stagger angle changes at $a = 9^\circ$ (Fig. 6 and Fig. 8). This change correspond to an increase of C_D, C_l' and C_d', and a decrease of the absolute value of C_L up to the single cylinder values. For $a = 10.5^\circ$ (Fig. 14), the downstream cylinder is partly embedded in the small cylinder wake which interaction with the cylinder boundary layer is weaker than in the previous flow regime ($a = 7.5^\circ$ case). The perturbation does no longer occur from the stagnation point of the

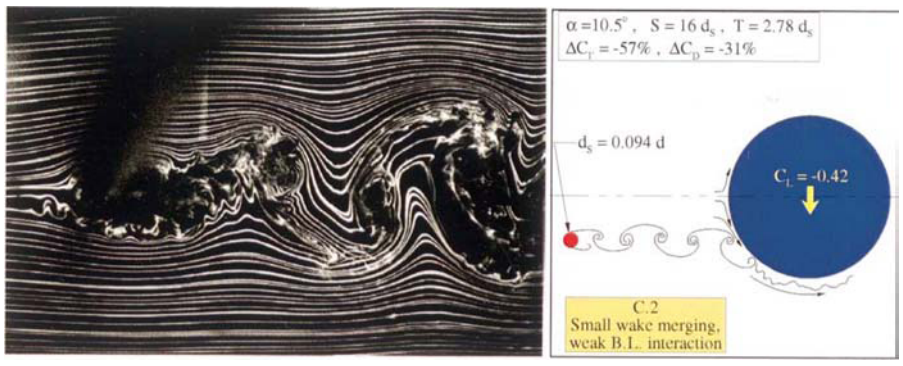

Fig. 14. Smoke-wire flow visualization and schematic of the flow pattern C.2 (small-wake merging flow regime with weak boundary-layer interaction); configuration $S/d = 1.5$, $a = 10.5^\circ$.

large cylinder (flow pattern C. 2).

When the wake completely bypasses the downstream cylinder, no more C_D reduction is observed. For $15^\circ < a < 40^\circ$, there is a compression of the streamlines between the downstream cylinder and the upstream cylinder wake, resulting in an increase in velocity of the local flow approaching the downstream cylinder and hence in a decrease of the Strouhal number (see Fig. 9). This is illustrated by the schematic of the flow pattern D identified as the outer-flow interaction configuration and corresponding to $a = 17^\circ$ (Fig. 15).

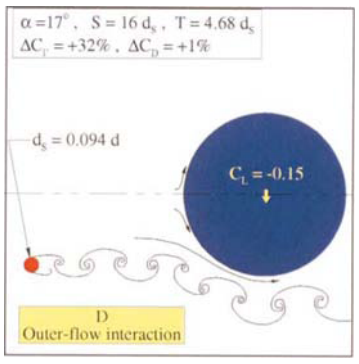

Fig. 15. Schematic of the flow pattern D identified as the outer-flow interaction configuration; $S/d = 1.5$, $a = 17^\circ$.

The flow patterns around a circular cylinder controlled by a small cylinder upstream can be classified according to the stagger angle. The characteristics of those patterns are summarized in Table 1.

Table 1. Definition of different flow regimes (see Fig. 8).

A Attached flow	A.1 Stable	$0^\circ < a < 2^\circ$	$0 < T/d_s < 0.3$
	A.2 Bi-stable	$2^\circ \le a \le 3^\circ$	$0.6 < T/d_s < 0.8$
B Small-wake splitting		$3^\circ < a < 5^\circ$	$0.8 < T/d_s < 1.4$
C Small-wake merging	C.1 Strong boundary-layer interaction	$5.5^\circ < a < 9^\circ$	$1.5 < T/d_s < 2.5$
	C.2 Weak boundary-layer interaction	$9.5^\circ < a < 11^\circ$	$2.6 < T/d_s < 3.1$
D Outer-flow interaction		$12^\circ < a < 40^\circ$	$3.3 < T/d_s < 10.3$
E Negligible interaction		$40^\circ < a < 90^\circ$	$10.3 < T/d_s < 16$

5. Conclusion

The passive control of unsteady forces induced on a circular cylinder (d = 25.4 mm) has been investigated. In the parametric study case, the flow was controlled using upstream small circular cylinders ($1.19 \le d_s \le 3.2$ mm). The position of each small cylinder was varied within the range $1.375 \le S/d \le 2.5$ and $0^\circ \le \alpha \le 90^\circ$. Important features have been observed on curves of mean lift and drag coefficients. Among these, a reduction of the mean drag of 48% occurring at a stagger arrangement, and the observation of two different C_L peaks for particular configurations are of prime interest. This indicates that two entirely different flow patterns are the cause. To clarify this argument, unsteady results are presented for the case d_s = 2.4 mm and S/d = 1.5 (or S/d_s = 16). At $\alpha = 6.5^\circ$, one observes a maximum reduction of 78% in the rms lift fluctuations. This leads to an instantaneous force vector which exhibits more steadiness, both in angle and amplitude. Moreover, at this stagger angle, the energy of the lift fluctuations at the shedding frequency is reduced by more than 99% compared with the single cylinder case (no control case). At $\alpha = 2^\circ$, a discontinuity in the unsteady forces occurred and was likely attributed to a bi-stable regime in the gap. Finally, a classification and sketches of the flow patterns have been made.

Acknowledgments

The support of the Canadian NSERC is gratefully acknowledged.

References

Bouak, F., Étude de l'Écoulement Autour de Structures Composées de Deux Cylindres, (1999), Ph.D. Thesis, Université Laval, Québec, Canada.

Bouak, F. and Lemay, J., Passive Control of the Aerodynamic Forces Acting on a Circular Cylinder, Exp. Thermal and Fluid Science, 16 (1998), 112-121.

Igarashi, T., Enhancement of Heat Transfer and Reduction of Drag of a Square Prism in an Air Stream, Proc. 10th Int. Heat Transfer Conf., vol. 6, (1994), 49-54.

Igarashi, T., Drag Reduction of a Square Prism by Flow Control Using a Small Rod, J. Wind Eng. and Ind. Aerodyn., 69-71 (1997), 141-153.

Igarashi, T., Visualization of Flow Around a Bluff Body Controlled by a Rod Set Upstream, 8th Int. Symp. on Flow Visualization (Sorrento, Italy), (2000), CD-ROM 101.1-101.6.

Lesage, F. and Gartshore, I. S., A Method of Reducing Drag and Fluctuating Side Force on Bluff Bodies, J. Wind Eng. and Ind. Aerodyn., 25 (1987), 229-245.

Moeller, M. J., Measurement of Unsteady Forces on a Circular Cylinder in Cross Flow at Subcritical Reynolds Numbers, (1982), Ph.D. Thesis, Mass. Inst. Tech., Cambridge, Massachusetts.

Niemann, H. J. and Hölscher, N., A Review of Recent Experiments of the Flow Past Circular Cylinders, J. Wind Eng. and Ind. Aerodyn., 33 (1990), 197-209.

Tsutsui, T. and Igarashi, T., Drag Reduction of a Circular Cylinder in an Air Stream, 4th Int. Colloquium on Bluff Body Aerodynamics & Applications (Bochum, Germany), (2000), 639-642.

West, G. S. and Apelt, C. J., Measurements of Fluctuating Pressures and Forces on Circular Cylinder in the Reynolds Number Range 10^4 to 2.5×10^5, J. Fluids Struc., 7 (1993), 227-244.

Zdravkovich, M. M., Flow around Circular Cylinders Volume 1, (1997), Oxford Science Publications.

Author Profile

Fethi Bouak: He studied in Mechanical Engineering and received his B.Sc. (1986) degree from National Polytechnic School of Algiers, Algeria, M.Sc. (1990) from Sherbrooke University in Sherbrooke, Canada and Ph.D. (1999) degree under the supervision of Prof. Jean Lemay from Laval University in Quebec, Canada. He worked as a research scientist in the department of Mechanical Engineering at Laval University and at the Royal Military College of Canada.

Jean Lemay: He received his B.Sc.A. (1983), M.Sc. (1986) and Ph.D. (1989) degrees in Mechanical Engineering from Laval University in Quebec, Canada. He has done the experimental work related to his Ph.D. at the CEAT of Poitiers, France, from 1985 to 1988, and during a short stay at Cambridge University, UK, in 1986. He is full professor and Head of the undergraduate program in the department of Mechanical Engineering at Laval University. He is also Head Manager of the Fluid Mechanics Laboratory. His research interest covers different problems related to turbulent shear flows, fluid-structure interactions and aerodynamics. He is particularly interested in the study of small scale turbulence, and active or passive control of jets, wakes and boundary layers.